Semina Ciências Exatas e Tecnológicas

e-ISSN 1679-0375
PHYSICS

ORIGINAL ARTICLE DOI 10.5433/1679-0375.2026.v47.52838

iThenticate

Laser-Assisted He-atom Scattering in Mixed Circular Polarized Field

Espalhamento de Átomos de Hélio Assistido por Laser em Campo de Polarização Circular Mista

Basanta Ghimire[1], Kishori Yadav[2], Suresh Prasad Gupta[2], Manish Pokhrel[1], Sharad Kumar Oli[1], Saddam Husain Dhobi[2]*

Received: August 22, 2025 *Received in revised form: January 9, 2026* *Accepted: February 18, 2026* *Available online: February 23, 2026*

ABSTRACT

The aim of this work is to study the scattering dynamics of electrons by helium screening and non-screening potentials in a mixed circular polarized laser field. For this, we developed a theoretical model using Volkov wave function of a mixed laser field, S-matrix, Bessel functions and Kroll and Watson approximation of the differential cross section (DCS). The developed model was numerically simulated using MATLAB programming language. The results show that DCS generally increases with separation distance and momentum transfer. For the case $N = M = 0$, DCS exhibits a sinusoidal variation with scattering angle. For $N = M = 1$, DCS increases with distance and momentum transfer, but decreases with scattering angle due to damping; interference peaks occur at specific phases for small angles, while at larger angles DCS shows interference behavior with phase-related decrease. For $N = M = 2$ and $N = M = 3$, DCS similarly increases with distance and momentum transfer, with scattering angle showing damping followed by interference beyond certain angles. Higher photon exchanges further lower DCS amplitude and enhance phase sensitivity. The findings highlight the significant role of laser phase and photon exchange in controlling electron-helium scattering dynamics.

keywords scattering dynamics, screening, Volkov wave, non-screening potentials, photon

RESUMO

O objetivo deste trabalho é estudar a dinâmica de espalhamento de elétrons por potenciais de hélio com blindagem e sem blindagem em um campo laser de polarização circular mista. Para isso, desenvolvemos um modelo teórico utilizando a função de onda de Volkov para um campo laser misto, a matriz S, funções de Bessel e a aproximação de Kroll e Watson para a seção de choque diferencial (DCS). O modelo desenvolvido foi simulado numericamente utilizando a linguagem de programação MATLAB. Os resultados mostram que a DCS geralmente aumenta com a distância de separação e a transferência de momento. Para o caso $N = M = 0$, a DCS apresenta uma variação senoidal com o ângulo de espalhamento. Para $N = M = 1$, a DCS aumenta com a distância e a transferência de momento, mas diminui com o ângulo de espalhamento devido ao amortecimento; picos de interferência ocorrem em fases específicas para pequenos ângulos, enquanto em ângulos maiores a DCS apresenta comportamento de interferência com diminuição relacionada à fase. Para $N = M = 2$ e $N = M = 3$, a DCS aumenta de forma semelhante com a distância e a transferência de momento, sendo que o ângulo de espalhamento apresenta amortecimento seguido de interferência além de certos ângulos. Trocas de fótons mais elevadas reduzem ainda mais a amplitude da DCS e aumentam a sensibilidade à fase. Os resultados destacam o papel significativo da fase do laser e da troca de fótons no controle da dinâmica de espalhamento elétron-hélio.

palavras-chave dinâmica de espalhamento, blindagem, onda de Volkov, potenciais não blindados, fótons

[1]Master, Department of Physics, Patan Multiple Campus, TU, Lalitpur, Nepal. basantaghimire730@gmail.com, manishpokhrel0626@gmail.com, oli.sharadkumar@gmail.com

[2]PhD, Department of Physics, Patan Multiple Campus, TU, Lalitpur, Nepal. yadavkishori70@gmail.com, guptasirphys@gmail.com, saddam@ran.edu.np

Introduction

Laser-assisted electron–atom scattering is a fundamental process for understanding how external electromagnetic fields modify collision dynamics at the quantum level. In such interactions, scattering arises from the coupling between charged particles and atomic targets. It is quantitatively described using quantum wave functions together with S-matrix and T-matrix formalisms, which determine transition probabilities between initial and final states (Bhatia, 2020; Schwartz, 2014).

Under intense laser fields, electron motion is well represented by the Volkov wave function. In addition, temperature-induced effects are incorporated through the thermal Volkov formalism. This approach allows a unified description of laser and thermal environments (Dhobi et al., 2024, 2025).

The differential cross section (DCS) remains the key observable. It provides the angular probability distribution of scattered electrons. Moreover, it reveals interference effects associated with photon absorption and emission during collisions (Benacquista, 2018).

Earlier investigations of laser-assisted electron scattering predominantly considered linearly polarized laser fields. These studies often neglected thermal effects. As a consequence, their relevance to realistic physical conditions is limited (Bhattacharya et al., 2002; Szymanowski & Maquet, 1998; Taj et al., 2010).

Although circular polarization has been explored in isolated cases, a systematic and comparative treatment remains absent in the literature. Electron–helium scattering under mixed circularly polarized laser fields has not been comprehensively analyzed. Such a treatment should incorporate screened and non-screened atomic potentials, laser phase effects, small and large angle regimes, and multi-photon exchanges beyond the single-photon limit.

The original contribution of this work lies in developing a comprehensive theoretical model. This model simultaneously accounts for these factors. In particular, photon exchange processes are extended from $N = M = 0$ to $N = M = 3$.

Through detailed numerical simulations, this study demonstrates how screening, photon number, laser phase, momentum transfer, and scattering geometry collectively govern DCS behavior.These results provide new predictive insights into controllable laser-assisted electron–helium scattering dynamics.

Materials and methods

To develop the model for the study of scattering dynamics of an electron in mixed circular laser field by helium atom. First, we consider the electron projected in two-color laser field is treated by Gordon-Volkov wave function (Volkov, 1935) and the initial states of the projectile electron are given in equation (1) according to:

$$X_p(R,t) = (2\pi)^{-3/2} \exp[-iE_p t + i\mathbf{p}\cdot\mathbf{R} - i\mathbf{p}\cdot\boldsymbol{\alpha}_1(t) - i\mathbf{p}\cdot\boldsymbol{\alpha}_m(t)]\,, \tag{1}$$

where $\mathbf{R}$ represents the position vector, and the quantities $\boldsymbol{\alpha}_k(t)$, with $k = 1$ and m, describe the classical oscillatory motion of the projectile electron in bicircular electric fields. They are defined in equations (2) and (3), following in Buica (2017) as presented below:

$$\boldsymbol{\alpha}_1(t) = \frac{\alpha_{01}}{\sqrt{2}}\left(\mathbf{e}_j \sin\omega_j t + \mathbf{e}_l \cos\omega_l t\right), \tag{2}$$

$$\boldsymbol{\alpha}_m(t) = \frac{\alpha_{0m}}{\sqrt{2}}\left(\mathbf{e}_j \sin\omega_m t + \mathbf{e}_l \cos\omega_m t\right). \tag{3}$$

where $\alpha_{0k} = \sqrt{I_k}/\omega_k^2$ is the peak amplitude and $I_k = E_{0k}^2$ is the peak laser intensity. The electronic Hamiltonian in atomic units for a helium atom is given in equation (4), by Varilla et al. (2019), is given by

$$\dot{H} = -\frac{1}{2}\nabla_{r_1}^2 - \frac{1}{2}\nabla_{r_2}^2 - \frac{2}{r_1} - \frac{2}{r_2} + \frac{1}{|\mathbf{r}_2 - \mathbf{r}_1|}. \tag{4}$$

The effective potential experienced by the electron arises from its interaction with the nucleus and the charge distribution of the second electron. It is mathematically described by equations (5) and (6), according to Varilla et al. (2019):

$$V(r) = -\frac{Z_1}{r} + \int \frac{\phi^2(r', Z_2)}{|\mathbf{r} - \mathbf{r}'|}\, dr', \tag{5}$$

$$V(r) = \frac{1 - Z_1}{r} + \frac{1}{r}\left[(1 + Z_2 r)\exp(-2Z_2 r)\right], \tag{6}$$

where, $\phi(r', Z_2) = \sqrt{\frac{Z_2^3}{\pi}}\exp(-Z_2 r)$, and Z_i is the effective charge that the electron experiment. For the non-screening potential, $Z_1 = Z_2 = 2$, as shown in equation (7) (Varilla et al., 2019):

$$V(r) = -\frac{1}{r} - \frac{1}{r}\left[(1 + 2r)\exp(-4r)\right]. \tag{7}$$

For the screening potential, $Z_1 = 2$ and $Z_2 = 2 - \frac{5}{16}$, as given in equation (8) (Varilla et al., 2019):

$$V(r) = -\frac{1}{r} - \frac{1}{r}\left[\left(1 + \frac{27}{16}r\right)\exp\left(-2\frac{27}{16}r\right)\right]. \tag{8}$$

Equations (7) and (8) establish the relationship between the reduced potential $U(r)$ and the effective potential $V(r)$, given by $U(r) = \frac{2mV(r)}{\hbar^2}$.

The analysis then proceeds from the scattering matrix defined in equation (9). This matrix is examined within the framework of high-energy scattering, following (Clarito, 2013):

$$S_{if}^{B1} = -i\int_{-\infty}^{+\infty} dt\langle\chi_i(t)|\Psi_n^m(t)\rangle\langle V(r,R)|X_i(t)\rangle\langle\chi_i(t)|\Psi_n^m(t)\rangle, \tag{9}$$

where $\Psi_n^m(t)$ is the unperturbed excited state of hydrogen with energy E_n, and $\chi_{i(f)}(t)$ is the Gordon–Volkov wave function representing both the initial and final states of the scattering electron. These states remain identical due to the free–free transition (Kroll & Watson, 1973):

$$S_{fi} = I - 2\pi i T = I - 2\pi i\int_{-\infty}^{\infty} dt\langle\chi_{p_f}|V(r,R)|\chi_{p_i}\rangle. \tag{10}$$

The second term of equation (10) is equivalent to the transition matrix. Accordingly, the transition matrix is obtained from this term by substituting the expressions for χ_{p_f} and χ_{p_i} from equations (1)–(3). This substitution is carried out within the framework of the spherical coordinate system, leading to the following expression:

$$\begin{aligned} T_{fi} &= -i\int_{-\infty}^{\infty} dt\,\langle\chi_{p_f}|V(r,R)|\chi_{p_i}\rangle \\ &= -i\int_{-\infty}^{\infty} dt\left[\int_0^{2\pi} d\phi\int_0^{\pi} d\theta\,\sin\theta\int_0^{\infty} dr\,r^2\,(2\pi)^{-3/2}\exp\Big(iE_{p_f}t - i\mathbf{p}_f\cdot\mathbf{R} + i\mathbf{p}_f\cdot\boldsymbol{\alpha}_1(t) + i\mathbf{p}_f\cdot\boldsymbol{\alpha}_m(t)\Big)\right. \\ &\left.\times\, V(r)\,(2\pi)^{-3/2}\exp\big(-iE_{p_i}t + i\mathbf{p}_i\cdot\mathbf{R} - i\mathbf{p}_i\cdot\boldsymbol{\alpha}_1(t) - i\mathbf{p}_i\cdot\boldsymbol{\alpha}_m(t)\big)\right]. \end{aligned} \tag{11}$$

On solving equation (11) with the assumption $\mathbf{q} = \mathbf{p}_f - \mathbf{p}_i$, we obtain

$$T_{fi} = \frac{1}{q}(2\pi)^{-2} I_r\exp\big(iqR\cos\theta\big)\int_{-\infty}^{\infty} dt\,\frac{\exp\big\{i(E_{p_f} - E_{p_i})t + iq[\alpha_1(t) + \alpha_m(t)]\cos\theta\big\}}{[\alpha_1(t) + \alpha_m(t) - R]}. \tag{12}$$

For simplicity, we assume $2\cos A\cos B = \cos(A+B) + \cos(A-B)$ in equation (12). There for, for the small angle approximation we take $2\cos A\cos B = \cos(A-B)$, and for the large angle approximation we take $2\cos A\cos B = \cos(A+B)$. Now from equation (12), for small angles we have $\exp[iq\alpha(t)] = \exp\big[iqR/2\cos(\omega t + \phi - \theta)\big]$, and for large angles $\exp[iq\alpha(t)] = \exp\big[iqR/2\cos(\omega t + \phi + \theta)\big]$. Also, using the Jacobi–Anger expansion after the angle approximation, with the involvement of Bessel functions (Dattoli et al., 1991) of the form

$$\exp(iz\cos\theta) = \sum_{n=-\infty}^{\infty} i^n J_n(z)\exp(in\theta), \tag{13}$$

Solving the integral part of equation (12), for a small angle, we get equation (14) as

$$\begin{aligned} I_t = \int_{-\infty}^{\infty} &\frac{\exp\big[i(E_{p_f} - E_{p_i})t\big]\sum_{N=-\infty}^{\infty}\Big[i^N J_N\Big(\frac{R_1 q}{2}\Big)\exp\big(iN(\omega_1 t + \phi_1 - \theta)\big)\Big]}{[\alpha_1(t) + \alpha_m(t) - R]} \\ &\times\sum_{M=-\infty}^{\infty}\Big[i^M J_M\Big(\frac{R_m q}{2}\Big)\exp\big(iM(\omega_m t + \phi_m - \theta)\big)\Big]. \end{aligned} \tag{14}$$

Solving the integral in equation (14) using the residue theorem to evaluate the contour integral, we obtain equation (15) in the form

$$I_t = \int_{-\infty}^{\infty} dt \, \frac{\exp\left[i(E_{p_f} - E_{p_i} + N\omega_1 + M\omega_m)t\right]}{\left(R_1\cos(\omega_1 t + \phi_1) + R_m\cos(\omega_m t + \phi_m) - R\right)}$$
$$= 2\pi i \sum_{\text{upper poles}} \frac{\exp\left[i(E_{p_f} - E_{p_i} + N\omega_1 + M\omega_m)z_k\right]}{-\left(R_1\omega_1\sin[(\omega_1 + \phi_1)z_k] + R_m\omega_m\sin[(\omega_m + \phi_m)z_k]\right)}, \tag{15}$$

where the poles z_k correspond to the resonant times at which constructive interference of the oscillating fields occurs. Now, substituting the value of equation (15) into equation (12) and solving, we obtain equation (16) for the small angle case as,

$$T_{fi}^{\text{small}} = \frac{1}{q}\, i(2\pi)^{-1} I_r \sum_{N=-\infty}^{\infty} i^N j_N\left(\frac{R_1 q}{2}\right) \sum_{M=-\infty}^{\infty} i^M j_M\left(\frac{R_m q}{2}\right)$$
$$\times \exp\left(iN\phi_1 - i(M+N)\theta + iM\phi_m - iqR\cos\theta\right)$$
$$\times \sum_{\text{upper poles}} \frac{\exp\left[i(E_{p_f} - E_{p_i} + N\omega_1 + M\omega_m)z_k\right]}{-\left(R_1\omega_1\sin[(\omega_1 + \phi_1)z_k] + R_m\omega_m\sin[(\omega_m + \phi_m)z_k]\right)}. \tag{16}$$

Similarly, for the large angle case, the transition matrix is given in equation (17) as

$$T_{fi}^{\text{large}} = \frac{1}{q}\, i(2\pi)^{-1} I_r \sum_{M=-\infty}^{\infty} i^M j_M\left(\frac{R_m q}{2}\right)$$
$$\times \exp\left(iN\phi_1 + i(M+N)\theta + iM\phi_m + iM\theta - iqR\cos\theta\right)$$
$$\times \sum_{\text{upper poles}} \frac{\exp\left[i(E_{p_f} - E_{p_i} + N\omega_1 + M\omega_m)z_k\right]}{-\left(R_1\omega_1\sin[(\omega_1 + \phi_1)z_k] + R_m\omega_m\sin[(\omega_m + \phi_m)z_k]\right)}. \tag{17}$$

Also have screening potential as expressed in equation (18) as

$$V(r) = -\frac{1}{r} - \frac{1}{r}\left[(1 + \tfrac{27}{16}r)\exp(-2\tfrac{27}{16}r)\right]. \tag{18}$$

In addition, from equation (18), we also have an integral part of equation (16) as expressed by:

$$I_r = \int_0^r dr\, r^2 \left\{-\frac{1}{r} - \frac{1}{r}\left[(1 + \tfrac{27}{16}r)\exp(-2\tfrac{27}{16}r)\right]\right\}. \tag{19}$$

Solving the integral in equation (19), we obtain the final result for the screening potential as shown in equation (20),

$$I_r^{\text{screen}} = \left(\frac{r^2}{2} + \frac{16r}{27} + \frac{128}{729}\right)\exp\left(-\frac{27}{8}r\right) + \frac{r^2}{2} - \frac{128}{729}. \tag{20}$$

Also, we have non-screening potential as shown in equation (21)

$$V(r) = -\frac{1}{r} - \frac{1}{r}\left[(1 + 2r)\exp(-4r)\right]. \tag{21}$$

Taking the integration in the same manner as for the screening case, the radial integral for the non-screening potential is obtained as shown in equation (22),

$$I_r^{\text{Non-Screen}} = \left(\frac{r^2}{2} + \frac{3r}{8} + \frac{3}{32}\right)\exp(-4r) + \frac{r^2}{2} - \frac{5}{32}. \tag{22}$$

Differential cross section

In scattering theory, the differential cross section (DCS) (Kavazović et al., 2021) is defined by equation (23) as:

$$\frac{d\sigma}{d\Omega} = \frac{m^2}{(2\pi\hbar^2)^2}\frac{p_f}{p_i}\left|T_{fi}\right|^2. \tag{23}$$

Also, with the exchange of photons, equation (23) is modified as shown in equation (24):

$$\frac{p_f}{p_i} = \left(1 - \frac{\hbar(N\omega_1 + M\omega_m)}{E_{p_i}}\right)^{1/2}, \tag{24}$$

where N and M are the photon exchanges that occur in each laser field, since we consider two laser fields.

On substituting $\frac{p_f}{p_i}$ from (24) into equation (23), we have

$$\frac{d\sigma}{d\Omega} = \frac{m^2}{(2\pi\hbar^2)^2}\left(1 - \frac{\hbar(N\omega_1 + M\omega_m)}{E_{p_i}}\right)^{1/2} |T_{fi}|^2. \tag{25}$$

Screened and non-screened potentials for $M = N = 0$

Substituting the screened radial integral given in equation (20) into the small angle transition matrix expression, equation (16), and inserting the resulting amplitude into equation (25), we obtain the differential cross section (DCS) for $N = M = 0$, given by:

$$\left(\frac{d\sigma}{d\Omega}\right)^{\text{small}}_{\text{screened}} = \frac{1}{(4\pi^2 q)^2}\left|\left\{\left(\frac{r^2}{2} + \frac{16r}{27} + \frac{128}{729}\right)\exp\left(-\frac{27}{8}r\right) + \frac{r^2}{2} - \frac{128}{729}\right\}\right.$$
$$\left.\times \exp(-iqR\cos\theta)\sum_{\text{upper poles}} \frac{1}{-\left(R_1\omega_1 \sin[(\omega_1 + \phi_1)z_k] + R_m\omega_m \sin[(\omega_m + \phi_m)z_k]\right)}\right|^2. \tag{26}$$

For the case $N = M = 0$, the analytical structure of the transition amplitude does not explicitly depend on the angular regime; consequently, equation (26) also describes the DCS for the screened potential in the large angle regime.

By substituting the radial integral from equation (22) into the expression for the small angle transition matrix, given in equation (17), and then inserting the resulting amplitude into equation (25), we obtain the corresponding differential cross section for N = M = 0, for the non-screened potential, denoted as

$$\left(\frac{d\sigma}{d\Omega}\right)^{\text{small}}_{\text{non-screened}} = \frac{1}{(4\pi^2 q)^2}\left|\left[\left(\frac{r^2}{2} + \frac{3r}{8} + \frac{3}{32}\right)\exp(-4r) + \frac{r^2}{2} - \frac{5}{32}\right]\right.$$
$$\left.\times \exp(-iqR\cos\theta)\sum_{\text{upper poles}} \frac{1}{-\left(R_1\omega_1 \sin[(\omega_1 + \phi_1)z_k] + R_m\omega_m \sin[(\omega_m + \phi_m)z_k]\right)}\right|^2. \tag{27}$$

Moreover, the same result as that shown in equation (27) is obtained for larger scattering angles in the non-screening case.

Screened and non-screened potentials for $M = N = 1$

Substituting equation (20) into equation (16) and inserting the resulting expression into equation (25) yields the differential cross section for $N = M = 1$ under the small angle approximation, as given in equation (28):

$$\left(\frac{d\sigma}{d\Omega}\right)^{\text{small}}_{\text{screened}} = \frac{1}{(64\pi^2)^2}\left(1 - \frac{(\omega_1 + \omega_m)}{E_{p_i}}\right)^{1/2}\left|i^3\left\{\left(\frac{r^2}{2} + \frac{16r}{27} + \frac{128}{729}\right)\exp\left(-\frac{27}{8}r\right) + \frac{r^2}{2} - \frac{128}{729}\right\}\right.$$
$$\times R_1 R_m q \exp(i\phi_1 - i2\theta + i\phi_m - iqR\cos\theta)$$
$$\left.\times \sum_{\text{upper poles}} \frac{1}{-\left(R_1\omega_1 \sin[(\omega_1 + \phi_1)z_k] + R_m\omega_m \sin[(\omega_m + \phi_m)z_k]\right)}\right|^2. \tag{28}$$

The DCS is obtained for larger angle of the same case (screened), equation (28), but the difference is only in the exponential term $\exp(i\phi_1 + i2\theta + i\phi_m - iqR\cos\theta)$.

Also, for the non-screened potential in the small angle approximation, the DCS is obtained by applying the above method, that is, by substituting equation (22) into equation (17) and then inserting the resulting amplitude into equation (25), yielding

$$\left(\frac{d\sigma}{d\Omega}\right)^{\text{small}}_{\text{non-screened}} = \frac{1}{(64\pi^2)^2}\left(1-\frac{(\omega_1+\omega_m)}{E_{p_i}}\right)^{1/2}\left|i^3\left[\left(\frac{r^2}{2}+\frac{3r}{8}+\frac{3}{32}\right)\exp(-4r)+\frac{r^2}{2}-\frac{5}{32}\right]\right.$$
$$\times R_1R_mq\exp(i\phi_1-i2\theta+i\phi_m-iqR\cos\theta)$$
$$\left.\times\sum_{\text{upper poles}}\frac{1}{-\left(R_1\omega_1\sin[(\omega_1+\phi_1)z_k]+R_m\omega_m\sin[(\omega_m+\phi_m)z_k]\right)}\right|^2. \tag{29}$$

For larger angle approximation and non-screening, the only different is the exponential term $\exp(i\phi_1 + i2\theta + i\phi_m - iqR\cos\theta)$, that is, if we substitute the exponential exponential term of equation (29), we obtain the expression for the large angle approximation.

Screened and non-screened potentials for $M = N = 2$

Substituting equation (20) into equation (16) and inserting the resulting expression into equation (25) yields the differential cross section for $N = M = 2$ under the small angle approximation, as given in:

$$\left(\frac{d\sigma}{d\Omega}\right)^{\text{small}}_{\text{screened}} = \frac{1}{(4096\pi^2)^2}\left(1-\frac{2(\omega_1+\omega_m)}{E_{p_i}}\right)^{1/2}\left|i^5\left\{\left(\frac{r^2}{2}+\frac{16r}{27}+\frac{128}{729}\right)\exp\left(-\frac{27}{8}r\right)+\frac{r^2}{2}-\frac{128}{729}\right\}\right.$$
$$\times(R_1R_m)^2q^3\exp(i2\phi_1-i4\theta+i2\phi_m-iqR\cos\theta)$$
$$\left.\times\sum_{\text{upper poles}}\frac{1}{-\left(R_1\omega_1\sin[(\omega_1+\phi_1)z_k]+R_m\omega_m\sin[(\omega_m+\phi_m)z_k]\right)}\right|^2. \tag{30}$$

For the large angle approximation with screening potential, the result in equation (30) remains the same, but the difference appears only in the exponential term, which becomes $\exp(i2\phi_1 + i4\theta + i2\phi_m - iqR\cos\theta)$.

By substituting equation (22) into equation (17) and using the resulting expression in equation (25), the DCS for $N = M = 2$, under the small angle approximation and for the non-screened potential, is obtained as:

$$\left(\frac{d\sigma}{d\Omega}\right)^{\text{small}}_{\text{non-screened}} = \frac{1}{(4096\pi^2)^2}\left(1-\frac{2(\omega_1+\omega_m)}{E_{p_i}}\right)^{1/2}\left|i^5\left[\left(\frac{r^2}{2}+\frac{3r}{8}+\frac{3}{32}\right)\exp(-4r)+\frac{r^2}{2}-\frac{5}{32}\right]\right.$$
$$\times(R_1R_m)^2q^3\exp(i2\phi_1-i4\theta+i2\phi_m-iqR\cos\theta)$$
$$\left.\times\sum_{\text{upper poles}}\frac{1}{-\left(R_1\omega_1\sin[(\omega_1+\phi_1)z_k]+R_m\omega_m\sin[(\omega_m+\phi_m)z_k]\right)}\right|^2. \tag{31}$$

For the large angle approximation with the non-screening potential, the result obtained in equation (31) remains unchanged, except for the exponential term, which becomes $\exp(i2\phi_1 + i4\theta + i2\phi_m - iqR\cos\theta)$.

Screened and non-screened potentials for $M = N = 3$

Similarly, substituting equation (20) into equation (16) and inserting the resulting expression into equation (25) yields the differential cross section for $N = M = 3$ under the small angle approximation, as given in:

$$\left(\frac{d\sigma}{d\Omega}\right)^{\text{small}}_{\text{screened}} = \frac{1}{(36864\pi^2\hbar^2)^2}\left(1-\frac{3(\omega_1+\omega_m)}{E_{p_i}}\right)^{1/2}\left|i^7\left[\left(\frac{r^2}{2}+\frac{16r}{27}+\frac{128}{729}\right)\exp\left(-\frac{27}{8}r\right)+\frac{r^2}{2}-\frac{128}{729}\right]\right.$$
$$\times(R_1R_m)^2q^3\exp(i3\phi_1-i6\theta+i3\phi_m-iqR\cos\theta)$$
$$\left.\times\sum_{\text{upper poles}}\frac{1}{-\left(R_1\omega_1\sin[(\omega_1+\phi_1)z_k]+R_m\omega_m\sin[(\omega_m+\phi_m)z_k]\right)}\right|^2. \tag{32}$$

Equation (32) is obtained for small angle approximation with screening potential, but the difference for the large angle approximation appears only in the exponential term, which becomes $\exp(i3\phi_1 + i6\theta + i3\phi_m - iqR\cos\theta)$.

Finally, substituting equation (22) into equation (17), and using the resulting in equation (25), the DCS for $N = M = 3$, under the small angle approximation and for the non-screened potential, is obtained as:

$$\left(\frac{d\sigma}{d\Omega}\right)^{\text{small}}_{\text{non-screened}} = \frac{1}{(36864\pi^2)^2}\left(1 - \frac{3(\omega_1+\omega_m)}{E_{p_i}}\right)^{1/2}\left|i^7\left[\left(\frac{r^2}{2}+\frac{3r}{8}+\frac{3}{32}\right)\exp(-4r) + \frac{r^2}{2} - \frac{5}{32}\right]\right.$$
$$\times (R_1R_m)^2 q^3 \exp(i3\phi_1 - i6\theta + i3\phi_m - iqR\cos\theta)$$
$$\left.\times \sum_{\text{upper poles}} \frac{1}{-\left(R_1\omega_1\sin[(\omega_1+\phi_1)z_k] + R_m\omega_m\sin[(\omega_m+\phi_m)z_k]\right)}\right|^2. \quad (33)$$

Also, equation (33) is the same for the large-angle approximation in the non-screening case, but the only difference appears in the exponential term, which becomes $\exp(i3\phi_1 + i6\theta + i3\phi_m - iqR\cos\theta)$.

Specifically, the small angle DCS described by equations (26)– (33), as well as that obtained under the large angle approximation, were calculated considering photon exchange orders from $N = M = 0$ (no field case) to $N = M = 3$ (three-photon exchange).

Results and Discussions

Computational details

The inter-particle separation (r) and the momentum transfer (q) were treated as control variables, while the scattering angle (θ) was restricted to a limited range. The laser phases (ϕ_1) and (ϕ_m) were examined independently. The oscillation amplitudes (R, R_1, and R_m) were kept constant, and the photon energies (ω_1 and ω_m) correspond to the two laser modes. The parameter values summarized in Table 1 were consistently employed in the MATLAB numerical simulations to analyze the dependence of the differential cross section (DCS) on the photon-exchange order, scattering geometry, and laser phases.

Table 1 - Computational parameters used in the simulations for the calculation of the DCS.

Parameter	Value / Range
Inter-particle separation (r)	0–1 Å
Momentum transfer (q)	0–1 eV
Scattering angle (θ)	0°–6°
Laser phase ϕ_1	0°–250°
Laser phase ϕ_m	0°–250°
Oscillation amplitude (R)	0.4 a.u.
Laser field amplitude (R_1)	1 a.u.
Laser field amplitude (R_m)	1 a.u.
Photon energy with phase ϕ_1 (ω_1)	1.17 eV
Photon energy with phase ϕ_m (ω_m)	2.17 eV

In each result presented, the parameter under consideration assumes the values listed in Table 1, while the remaining quantities are maintained at their reference values. Unless otherwise specified, the fixed parameters are $r = 1$, $q = 0.5$, $\theta = 5°$, $\theta_1 = 22.5°$, and $\theta_m = 20°$.

DCS results for the screened and non-screened potentials for $N = M = 0$

The DCS at large angle, as a function of inter-particle separation, momentum transfer, and scattering angle for the screening and non-screening potentials at $N = M = 0$, using the parameters listed in Table 1, is shown in Figure 1. Since the developed equation is the same for both the large and small angle approximations, see equation (26), the result is the same regardless of the approximation used. In addition, to make clear which approximation we are using, we explicitly mention the large angle approximation.

Figure 1 - Large angle DCS with: (a) distance separation, (b) momentum transfer, and (c) scattering angle of screening and non-screening potential $N = M = 0$.

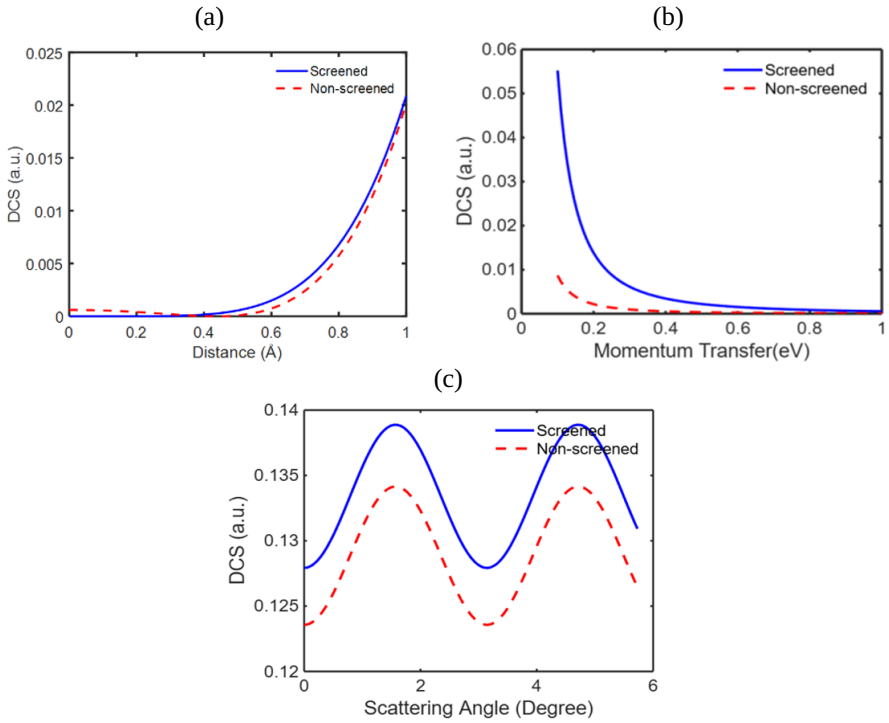

Figure 1(a) illustrates the variation of DCS with separation distance for both screening and non-screening helium potentials. The results show that the DCS increases with increasing separation distance. For distances greater than approximately 0.4 Å, the screening effect dominates, resulting in higher DCS values compared to the non-screening case. However, for distances below 0.4 Å, the non-screening effect becomes dominant, indicating a transition point at around 0.4 Å, where the nature of interaction shifts. This behavior suggests that at shorter distances, the bare potential (non-screening) plays a more significant role due to stronger Coulomb interactions, while at larger distances, the screened potential becomes more influential due to the weakening of direct interactions and the increasing role of field shielding.

Furthermore, the behavior of the electron–helium interaction under a laser field is consistent with the nature of the DCS, which is increasing with distance and field influence. Notably, at a separation of around 0.9 Å, the DCS values for both screening and non-screening cases begin to converge, indicating that the projectile electron field starts to dominate over the potential fields of both the target and the screened interaction. This convergence implies a region where the differences between the screened and non-screened interactions diminish due to the dominant role of the incident electron's field.

Figure 1(b) shows that the DCS decreases with increasing momentum transfer for both screening and non-screening cases.The DCS for the screening case remains consistently higher than that of the non-screening case.

This behavior can be explained by the interaction between the projectile electron and the target field. In the screening case, the field of the target is stronger due to the presence of screening, which prevents the low-energy projectile electron from penetrating deeply. As the energy of the projectile increases, it gradually overcomes the screening potential, allowing it to approach the target more closely. However, this increased energy causes the DCS to decrease, eventually reaching a minimum as the interaction strength diminishes. In contrast, in the non-screening case, the target field is inherently weaker. Even low-energy projectile electrons can approach the target more closely, resulting in lower DCS values from the start. As momentum transfer increases, the interaction remains weaker compared to the screened case. Overall, this trend indicates that the DCS is inversely related to the interaction strength: lower DCS corresponds to stronger interactions, while higher DCS reflects weaker interactions. This confirms that the interaction dynamics between particles are significantly influenced by the nature of the field (screened versus non-screened) and the momentum of the incident electron.

Figure 1(c) presents the variation of DCS with scattering angle. The results indicate that, at small scattering angles, the DCS for the screening case is higher than that for the non-screening case under the same projectile electron energy. This suggests that scattering angle significantly affects the interaction behavior in both cases, with the screened potential enhancing the DCS more prominently. The observed peak in DCS is attributed to resonance effects between the projectile and the target in the presence of a laser field. The resonance amplitude is greater for the screening case compared to the non-screening case, reflecting a stronger interaction.

DCS results for the screened and non-screened potentials for $N = M = 1$

By analyzing the development of equation (28), for the case of single photon exchange, it becomes possible to distinguish the modifications induced by the laser field compared to the field-free case where no photon exchange occurs. This comparison provides important insights into how screening effects, photon exchange, and angular dependence govern DCS behaviors in laser-assisted scattering, and is shown in Figure 2 for small angle.

Figure 2 - Screening and Non-Screening DCS with (a) distance separation, (b) momentum transfer, (c) scattering angle, (d) phase of first, and (e) phase of second laser for $N = M = 1$ at small angle.

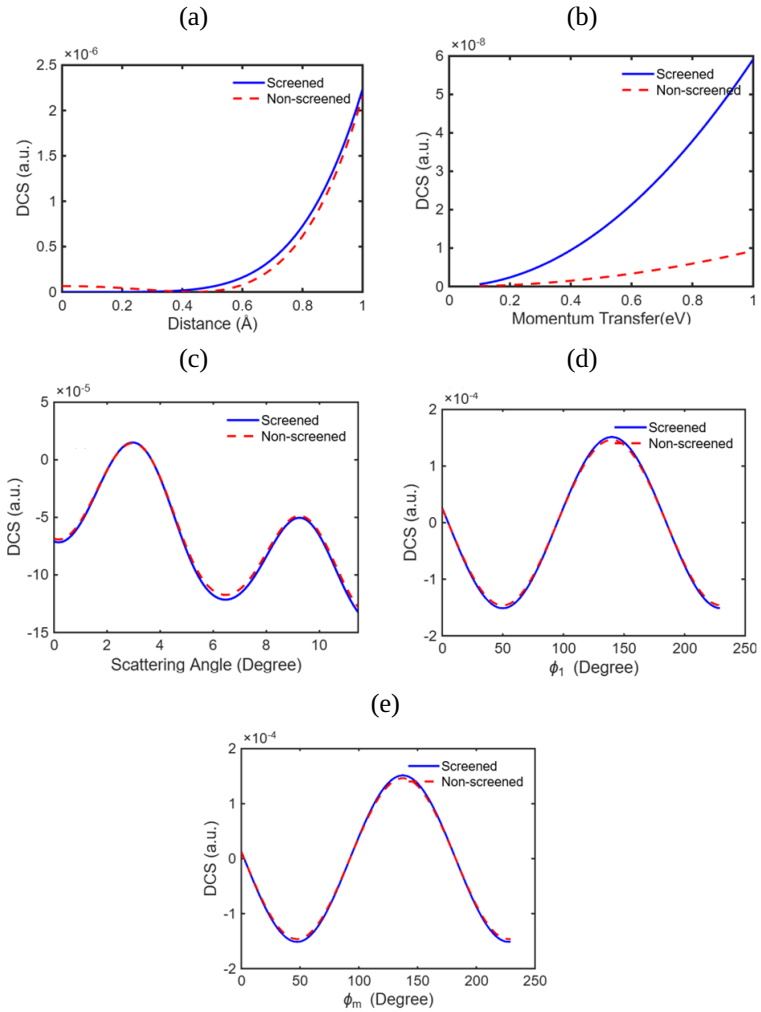

Figure 2(a) shows the DCS as a function of separation distance for the single-photon exchange case. It reveals a similar trend to that seen in the non-photon-exchange case, but with lower DCS values overall. This reduction occurs because photon exchange reduces the net energy between the projectile and target, thereby diminishing the interaction amplitude and resulting in lower DCS values.

Figures 2(b) and 2(c) illustrating that for momentum transfer and scattering angle, the DCS for single photon exchange is consistently lower than for non-exchanges photons, particularly at small angles. Notably, Figure 2(c) shows a damping-like behavior in the DCS with respect to the scattering angle, which arises due to the influence of the Bessel function, a characteristic of photon-exchange processes.

This damping behavior is absent in the non-photon-exchange case, where no photon exchange occurs and thus Bessel functions are not involved. These observations collectively confirm that single-photon exchange, screening effects, and scattering angle significantly influence the nature and strength of the electron–atom interaction in laser-assisted scattering scenarios.

Figure 2(d), illustrates the nature of the e–He interaction in the presence of a laser field, where the phase of one laser is varied while the other remains fixed. Conversely, Figure 2(e), shows the reverse scenario, where the second laser phase is varied and the first is held constant. The DCS is observed to vary with the phase difference, revealing regions where the DCS values remain constant over certain phase intervals and other regions where distinct phase-dependent variations occur. Notable phase-sensitive changes in the DCS appear around 50° and between 100° and 150°, particularly at small scattering angles. This behavior highlights the sensitivity of the DCS to relative phase shifts in the laser-assisted interaction process. Notable phase-sensitive changes in the DCS appear around 50° and between 100° and 150°, particularly at small scattering angles. This behavior highlights the sensitivity of the DCS to relative phase shifts in the laser-assisted interaction process. The larger angle DCS as a function of inter-particle separation, momentum transfer, and scattering angle for the shielding and non-shielding potentials at $N = M = 1$, are shown in Figure 3.

Figure 3 - Screening and Non-screening DCS with (a) scattering angle, (b) phase of first laser and, (c) phase of second laser for $N = M = 1$ at large angle.

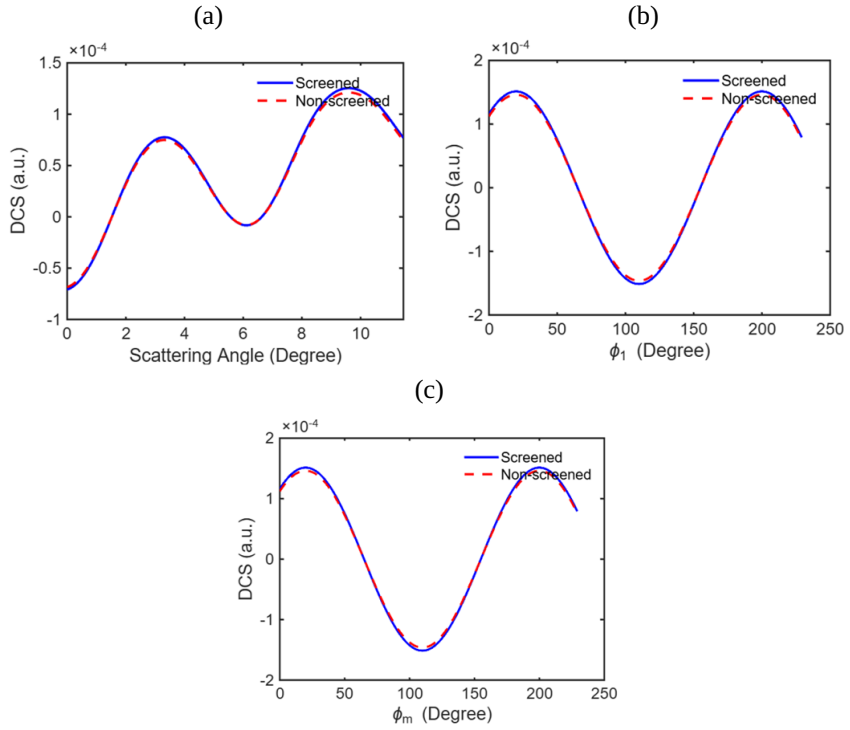

Figure 3(a) presenting the DCS behavior for the single photon exchange case as a function of scattering angle and phase. The results indicate that, unlike at small angles, the DCS increases with increasing scattering angle, and the DCS values at large angles are higher than those at small angles. Figures 3(b) and 3(c) further demonstrate the variation of DCS with phase for large-angle scattering. Interestingly, the DCS shows an opposite phase-dependent behavior at large angles compared to small angles, suggesting a reversal in the interaction field amplitude. These findings imply that laser phase effects become more pronounced at larger angles, altering the DCS in a manner opposite to that observed at small angles. This reversal may be attributed to the interference patterns induced by phase variation, which influence the constructive and destructive contributions of the laser-dressed interaction at different angular regimes.

DCS results for the screened and non-screened potentials for $N = M = 2$

The small angle DCS as a function of inter-particle separation, momentum transfer, and scattering angle for the screening and non-screening potentials at $N = M = 2$, using the parameters listed in Table 1. The investigation of electron–helium scattering in the presence of an external laser field becomes increasingly

complex when two exchange photons are considered. Unlike the single-photon case, where damping behavior is mainly governed by Bessel function contributions, at small scattering angles, the DCS shows distinct features such as damping, peaking, and resonance-like behavior, which are closely linked to the interference of laser phases and the relative role of screening. These characteristics reveal that the DCS is highly sensitive to angular variations and phase conditions, making the two-photon exchange regime essential for understanding how higher-order photon exchange modifies the nature of electron–atom interactions under laser influence, as can be seen in Figure 4.

Figure 4 - Screening and Non-Screening DCS with (a) distance separation, (b) momentum transfer, (c) scattering angle, (d) phase of first laser and, (e) phase of second laser for $N = M = 2$ at small angle.

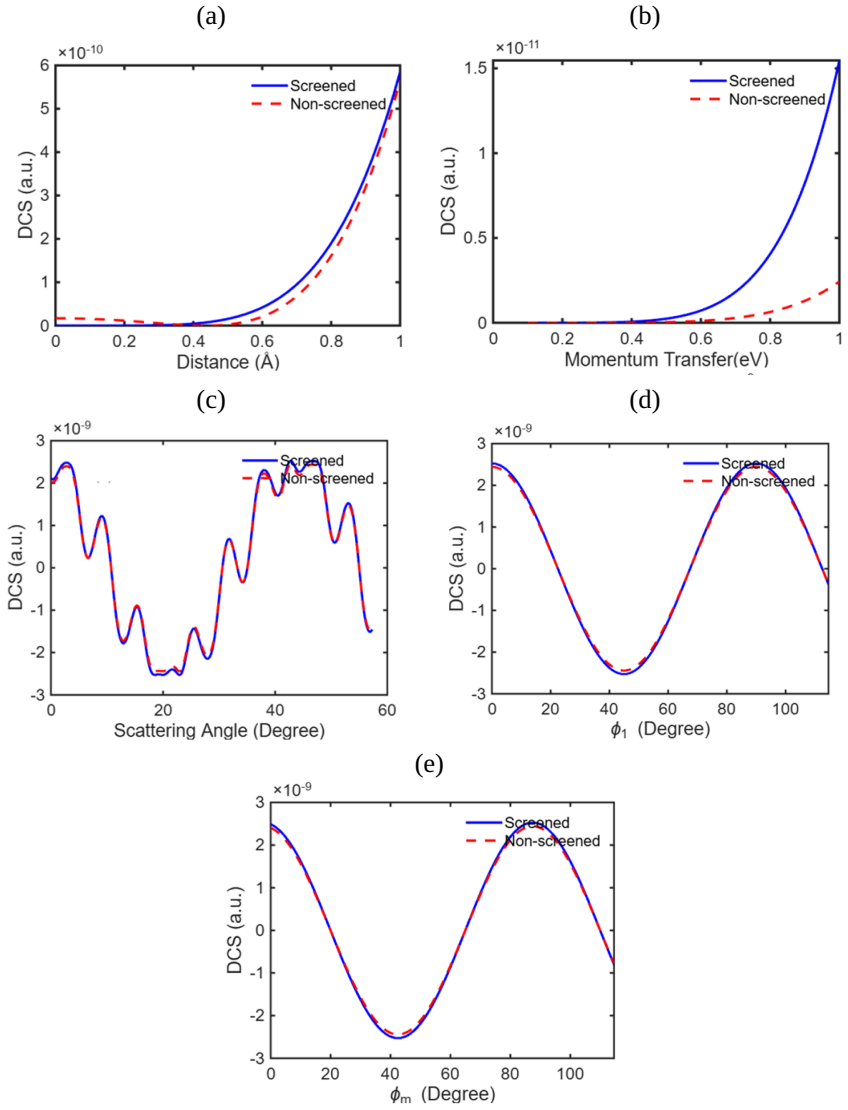

Figure 4(a) presents the DCS behavior for the two exchange photons at small scattering angles under. The results show that the overall nature of the DCS with respect to distance separation and momentum transfer remains qualitatively similar to that observed for the single exchanges photon case at small angles. However, the DCS as a function of scattering angle, reveals some distinct features. For angles below $20°$, the DCS exhibits a damping-like decrease, indicating reduced scattering probability as the angle becomes smaller. Beyond $20°$, the DCS exhibits a damping-like decrease, indicating reduced scattering probability as the angle becomes smaller. Beyond $20°$, the DCS starts to increase, reaching a maximum around $40°$, and then follows a repeating pattern similar to that below $20°$. This behavior reflects a resonance condition occurring when the projectile approaches the target closely under the influence of mixed laser phases, producing a small DCS peak. The damping and peaking effects are phase-driven and arise due to the interference pattern created by the superposition of laser fields, as also reflected in Figure 3(c).

Additionally, the overall amplitude of DCS for two exchanged photons is observed to be lower than that for single exchanged photons. This reduction is attributed to the fact that two-photon exchange induces stronger modulation, thereby suppressing the oscillation of the e–He interaction, which reduces the overall scattering probability. A comparison between the screening and non-screening cases shows minor differences: around 20°, the non-screening DCS is slightly higher, while around 40°, the screening DCS becomes dominant. This indicates that screening effects are angle-dependent and more pronounced in certain scattering regimes. Figures 4(d) and 4(e) illustrate the behavior of the DCS with respect to the laser phases ϕ_1 and ϕ_m for the mixed laser field in the two exchanged photons case. The nature of the DCS variation with phase is generally similar in both configurations, but a slight shift in the peak positions is observed, indicating that the relative phase between the laser components can influence the resonance conditions in the scattering process. Moreover, changes in the laser phase also cause variations in the DCS amplitude, where, at certain phases, the DCS for the screening case exceeds that of the non-screening case, and at other phases, the reverse occurs. This confirms that the laser phase plays a significant role in controlling and guiding the e–He scattering interaction.

The larger angle DCS is presented as a function of inter-particle separation, momentum transfer, and scattering angle for the screening and non-screening potentials at $N = M = 2$, using the parameters listed in Table 1. When extending the analysis of two-photon exchange to larger scattering angles, the DCS reveals new and contrasting behaviors compared to the small angle regime. While the overall dependence on distance separation and momentum transfer remains comparable, the angular distribution shifts, with resonance peaks moving toward higher scattering angles. This shift highlights the role of angular dependence in enhancing resonance structures. Moreover, the DCS response to laser phase exhibits a striking reversal effect: the phase dependence at large angles contrasts with that observed at small angles, pointing to a field-driven interference reversal that alters both the amplitude and direction of the scattering signal. The amplitude variations also differ between the two regimes, demonstrating that scattering at larger angles is strongly influenced by both angular position and laser phase, further underlining the sensitivity of laser-assisted scattering to external field conditions. DCS with scattering angle and phase for screening and non-screening effects was shown in Figure 5.

Figure 5 - Screening and Non-screening DCS with (a) scattering angle, (b) phase of first laser and, (c) phase of second laser for $N = M = 2$ at large angle.

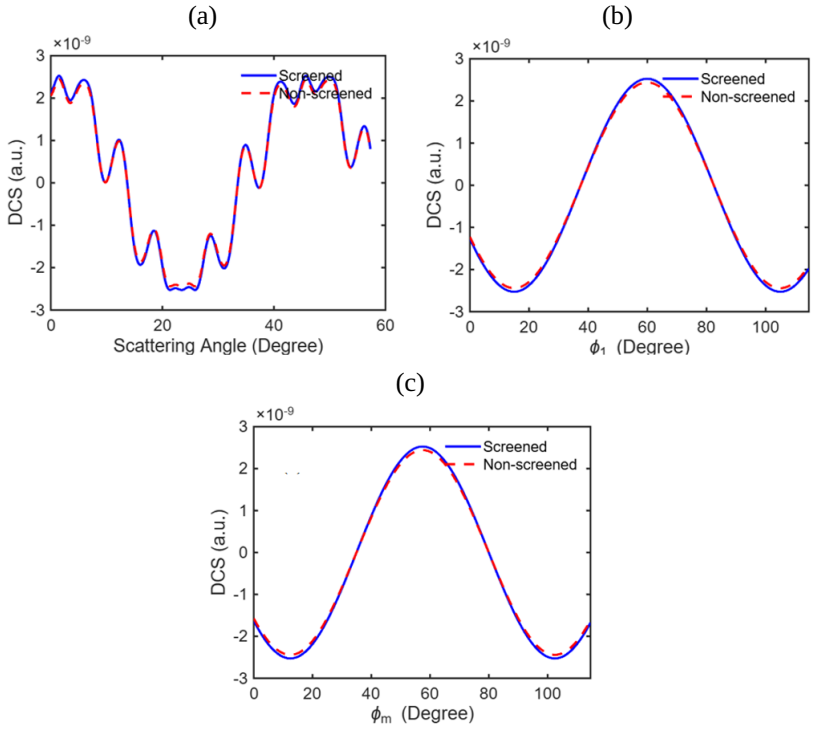

Figure 5(a) show that the DCS dependence on distance, and similarly, the results in Figure 5(b), show that the momentum transfer remains similar in nature and amplitude to that observed in the case of small angles (as in the previous parts of Figure 4). However, at larger angles, the DCS peaks are shifted to higher scattering angles compared to the peaks in Figure 4(c), indicating an increase in angle-dependent resonance. Importantly, Figures 5(b) and 5(c), display the DCS variation with laser phase at large angles, which shows an opposite trend when compared to the small-angle phase behavior in Figures 4(d) and 4(e). This indicates a phase inversion effect between small and large angles, i.e., the field amplitude and interference structure vary with the angle, altering the DCS in opposite directions. Furthermore, the DCS amplitudes at larger angles for two exchanged photons differ from those at small angles, further emphasizing that both the angle and the laser phase strongly modulate the scattering process in laser-assisted electron–atom interactions.

DCS results for the screened and non-screened potentials for $N = M = 3$

The small angle DCS is shown in Figure 6 as a function of inter-particle separation, momentum transfer, and scattering angle for the screening and non-screening potentials at $N = M = 3$, using the parameters listed in Table 1, are illustrated in Figure 6. For three-photon exchange, electron–helium scattering under a laser field shows a lower differential cross section compared to lower photon exchanges, indicating reduced scattering probability. At small angles, the overall DCS trend resembles the two-photon exchange case but with suppressed amplitude. Notably, the DCS exhibits a double-peak pattern in response to the laser phase, highlighting stronger interference effects and enhanced phase sensitivity. These results emphasize that the scattering behavior is strongly influenced by photon number, laser phase, and scattering angle, offering potential control over the interaction dynamics.

Figure 6 - Screening and Non-Screening DCS with (a) distance separation, (b) momentum transfer, (c) scattering angle, (d) phase of first laser and, (e) phase of second laser for $N = M = 3$ at small angle.

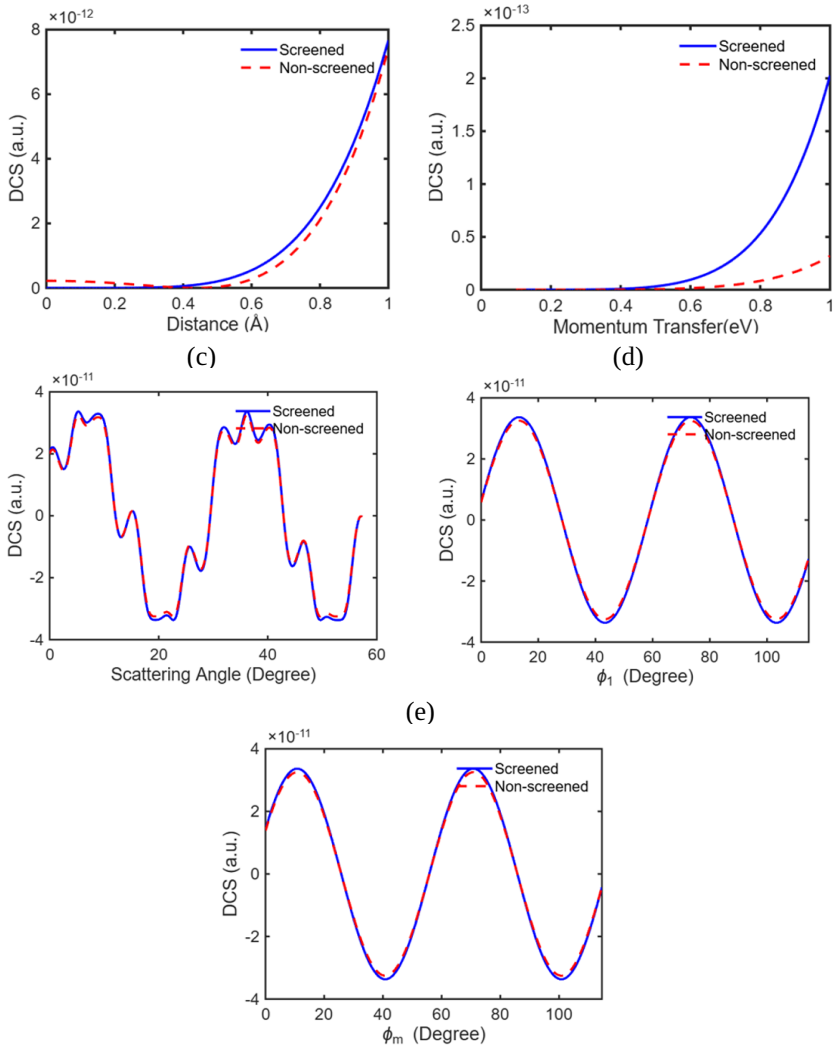

Figures 6(a)– 6(c) show the DCS behavior at small scattering angles for the three exchange photons case. The overall trend of DCS remains similar to the two exchange photons case, but with noticeably lower amplitude, indicating a reduction in scattering probability as the number of exchanged photons increases. This decreasing amplitude is due to the fact that higher-order photon exchange processes further reduce the oscillatory strength of the e–He interaction. Figures 6(d) and 6(e) explore the DCS variation with laser phase for $N = M = 3$.

At small angles, the overall DCS trend resembles the two-photon exchange case but with suppressed amplitude. Notably, the DCS exhibits a double-peak pattern in response to the laser phase, highlighting stronger interference effects and enhanced phase sensitivity. These results emphasize that the scattering behavior is strongly influenced by photon number, laser phase, and scattering angle, offering potential control over the interaction dynamics.

The behavior shows a distinct difference compared to the same phase variation patterns observed in the $N = M = 2$ case at both small and large angles. Most notably, within the phase interval of 0° to 100°, two clear DCS peaks are observed in the three-photon exchange case. This double-peak structure is absent in both the single-exchanges and two-exchange photon cases. These double peaks suggest that multi-photon interactions $N = M = 3$ induce stronger interference effects between the laser fields and the scattering system, enhancing the phase sensitivity of the interaction. This enhanced sensitivity further supports the conclusion that laser phase, number of exchanged photons, and scattering angle collectively influence the DCS pattern, offering potential control parameters for tuning e–He interactions in laser-assisted scattering processes.

The larger angle DCS as a function of inter-particle separation, momentum transfer, and scattering angle for the screening and non-screening potentials at $N = M = 2$, using the parameters listed in Table 1. For three-photon exchange at large scattering angles, the electron–helium differential cross-section slightly decreases, and the scattering peak shifts due to angular-dependent resonance effects. Laser phase variations show similar patterns to small angles, indicating that phase sensitivity is largely preserved in higher-order photon interactions. These results suggest that multi-photon processes dominate the scattering behavior, while scattering geometry and photon number together shape the DCS trends. The interaction of an electron and a helium atom in a laser field for screening and non-screening is shown with scattering angle and passes of two lasers, see Figure 7.

Figure 7 - Screening and Non-screening DCS with (a) scattering angle, (b) phase of first laser and, (c) phase of second laser for $N = M = 3$ at large angle.

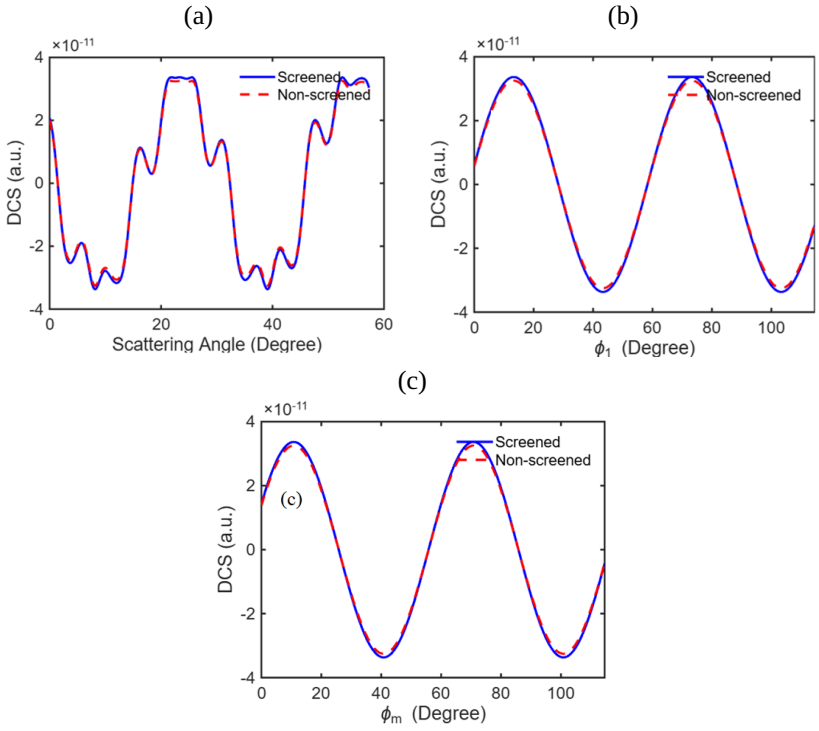

Figure 7(a) shows the DCS as a function of the scattering angle, Figure 7(b) shows the DCS with variation in the laser phase ϕ_1, and Figure 7(c) shows the DCS with variation in the laser phase ϕ_m. The DCS variation with distance and momentum transfer follows a similar trend to that of the small-angle case shown in Figure 6, particularly Figure 6(c).

However, the overall DCS amplitude is slightly lower, suggesting that the scattering probability decreases at larger angles for the same photon exchange condition. Additionally, a shift in the DCS peak is observed: the scattering peak moves toward a lower angle compared to the peak in Figure 6(c). This shift indicates that resonance conditions and angular dependence are affected by the scattering geometry even when the photon exchange number remains the same ($N = M = 3$).

Furthermore, when examining the effect of the laser phase for both lasers, the DCS variation with phase is found to be almost identical to that of the small-angle case for $N = M = 3$. This consistency implies that laser phase sensitivity in the three-photon exchange regime is less dependent on the scattering angle than in lower photon exchange scenarios ($N = M = 1$ or 2), reinforcing the idea that multi-photon processes dominate the interaction symmetry.

This study is purely theoretical and is based on model-dependent equations without experimental validation. The analysis is restricted to circularly polarized laser fields and non-relativistic regimes, limiting the generalizability of the results. Higher-order photon interactions, as well as the effects of linearly or elliptically polarized fields, have not been considered in the model. Additionally, quantum electrodynamical corrections, target recoil effects, and relativistic corrections, which may become significant at high energies, are omitted. The conclusions drawn from the DCS behavior under various photon exchange conditions ($N = M = 0$ to 3), laser phases, and angular variations should therefore be interpreted as predictive trends within the scope of the model rather than as definitive physical outcomes. Further experimental validation and extended theoretical modeling are necessary to confirm and generalize these findings.

Conclusion

This study explored how laser fields influence electron scattering from helium atoms, comparing two types of interaction potentials: screening and non-screening. The results show that screening reduces the effective interaction between the electron and the atom at larger distances, while the non-screening potential dominates at short range. The scattering behavior depends strongly on parameters such as interparticle distance, momentum transfer, scattering angle, and laser phase.

The findings indicate that photon exchange with the laser field reduces the overall scattering probability while increasing sensitivity to the laser phase, thereby enabling control over the interaction process. The differences observed between the screening and non-screening cases emphasize the importance of including electron shielding effects in such analyses.

Although this work provides valuable theoretical insights, it is subject to limitations, including the assumption of non-relativistic conditions, the restriction to circular polarization, and the absence of experimental validation. Future research should extend the model to incorporate more realistic physical conditions and seek experimental confirmation of the theoretical predictions. Overall, this study contributes to the understanding of laser-assisted atomic collisions and highlights potential avenues for controlling such interactions through laser parameter manipulation.

Acknowledgments

Authors would like all faculties and non-faculties of Department of physics, patan multiple campus, Tribhuvan university, Patandhoka, Lalitpur for providing all laboratories facilities and motivations during this research.

Author Contributions

B. Ghimire and **S. H. Dobhi**: conceptualization, data curation, formal analysis, investigation, methodology, original draft. **K. Yadav** and **S. P. Gupta**: validation, visualization, revision, and editing. **M. Pokhrel** and **S. K. Oli**: data curation, formal analysis, revision, and editing.

Conflicts of Interest

Authors has no conflict of interest.

References

Benacquista, M. J. (2018). *Classical mechanics*. Springer. http://www.springer.com/gp/book/9783319687797

Bhatia, A. K. (2020). Scattering and its applications to various atomic processes. *Atoms*, *8*(4), 78. https://doi.org/10.3390/atoms8040078

Bhattacharya, M., Malakar, B., & Sarkar, S. (2002). Scattering of electron by hydrogen atom in the presence of two laser fields. *Physica Scripta*, *66*(3), 208–214. https://doi.org/10.1238/Physica.Regular.066a00208

Buica, G. (2017). Circular dichroism in angular distribution of electron-hydrogen scattering in a two-color bicircular laser field. *Physical Review A*, *98*(5), 053427. https://doi.org/10.1103/PhysRevA.98.053427

Clarito, S. (2013). *The scattering matrix* [Master's thesis, Karlstad University]. https://kau.diva-portal.org/smash/record.jsf?pid=diva2:1662818

Dattoli, G., Torre, A., Lorenzutta, S., Maino, G., & Chiccoli, C. (1991). Theory of generalized bessel functions. ii. *Il Nuovo Cimento B*, *106*(1), 21–51. https://doi.org/10.1007/BF02723125

Dhobi, S. H., Yadav, K., Gupta, S. P., Nakarmi, J. J., & Jha, A. K. (2024). Differential cross section with volkov-thermal wave function in coulomb potential. *Atom Indonesia*, *1*(1), 19–25. https://atomindonesia.brin.go.id/index.php/aij/article/view/1309/1107

Dhobi, S. H., Yadav, K., Gupta, S. P., Nakarmi, J. J., & Jha, A. K. (2025). Non-monochromatic laser-assisted scattering in thermal environment. *Journal of the Nigerian Society of Physical Sciences*, *7*(1), 2345. https://doi.org/10.46481/jnsps.2025.2345

Kavazović, K., Čerkić, A., & Milošević, D. B. (2021). Electron-molecule scattering in a bichromatic elliptically polarised laser field: Plateau structures and two-centre interference minima. *Molecular Physics*, *119*(14), e1948123. https://doi.org/10.1080/00268976.2021.1948123

Kroll, N. M., & Watson, K. M. (1973). Charged-particle scattering in the presence of a strong electromagnetic wave. *Physical Review A*, *8*, 804–809. https://doi.org/10.1103/PhysRevA.8.804

Schwartz, M. D. (2014). *Quantum field theory and the standard model*. Cambridge University Press. https://ia601404.us.archive.org/22/items/quantum-field-theory-and-the-standard-model-by-schwartz-m.-d.-z-lib.org/Quantum_Field_Theory_and_the_Standard_Model_by_Schwartz_M.D._z-lib.org.pdf

Szymanowski, C., & Maquet, A. (1998). Relativistic signatures in laser-assisted scattering at high field intensities. *Optics Express*, *2*(7), 262–267. https://doi.org/10.1364/OE.2.000262

Taj, S., Manaut, B., Attaourti, Y., Elhandi, S., & Oufni, L. (2010). Coulomb scattering of an electron in strong laser fields. *Moroccan Journal of Condensed Matter*, *12*(3), 1–12. https://doi.org/10.34874/PRSM.mjcm-vol12iss3.291

Varilla, L. A., Pitalua, D. P., & Hoyos, F. T. (2019). Modeling a helium atom from a collision of an electron with an ionized helium atom. *Journal of Physics: Conference Series*, *1386*, 012119. https://doi.org/10.1088/1742-6596/1386/1/012119

Volkov, D. M. (1935). Über eine klasse von lösungen der diracschen gleichung. *Zeitschrift für Physik*, *94*(3–4), 250–260. https://doi.org/10.1007/BF01331022